energies

MDPI

Article

A Combined CFD-FEM Approach to Predict Fluid-Borne Vibrations and Noise Radiation of a Rotary Vane Pump

Timm Hieronymus [1,*], Thomas Lobsinger [1] and Gunther Brenner [2]

[1] Robert Bosch Automotive Steering GmbH, Richard-Bullinger-Straße 77, 73527 Schwaebisch Gmuend, Germany; thomas.lobsinger@bosch.com
[2] Institute of Applied Mechanics, Clausthal University of Technology, Adolph-Roemer-Straße 2A, 38678 Clausthal-Zellerfeld, Germany; gunther.brenner@tu-clausthal.de
* Correspondence: timm.hieronymus@bosch.com

Abstract: The rising demand for lower noise emissions of car ancillary units due to electrification and higher customer expectations regarding driving comfort results in the need for more silent car components. Hydraulic driven car components in particular are often identified as a major source of noise in the system. Therefore, it is mandatory to investigate the noise sources inside the hydraulic system. In this work, a combined CFD-FEM approach is applied to estimate the flow-induced noise radiation of a mechanically driven transmission pump. To achieve this goal, the mapping procedure to hand over the pressure field from the CFD to the FEM mesh must be valid. For this purpose, the error during the mapping process is evaluated and different parameters, which influence the mapping results, are analyzed. Additionally, the impact of the time step size and the length of the time signal on the frequency resolution of the force signal is investigated to get an appropriate excitation force for the vibroacoustic simulation. Subsequently, a force analysis and a structural FEM simulation are performed to identify which flow phenomenon contributes most to the excitation of the pump housing. Specific locations in the pump with high loads are pointed out. In a final step, the results of the vibroacoustic model are compared to acceleration and sound pressure level measurements of the pump performed in a hemi-anechoic room.

Keywords: rotary vane pump; NVH; noise radiation; CFD; FEM; vibroacoustic

Citation: Hieronymus, T.; Lobsinger, T.; Brenner, G. A Combined CFD-FEM Approach to Predict Fluid-Borne Vibrations and Noise Radiation of a Rotary Vane Pump. *Energies* **2021**, *14*, 1874. https://doi.org/10.3390/en14071874

Academic Editor: Satoru Okamoto

Received: 8 March 2021
Accepted: 26 March 2021
Published: 29 March 2021

1. Introduction

Automated car transmissions have high demands of power, reliability, low fuel consumption and low noise emissions. On the one hand, for most of these requirements a hydraulic, positive displacement pump is a suitable power supply. This kind of pump is able to provide high power, high reliability and lubrication of the system. Therefore, positive displacement pumps, especially rotary vane pumps, are often applied as power supplies in automated transmissions [1,2]. On the other hand, mechanically driven transmission pumps typically lead to an increased fuel consumption and to high noise emissions.

Nowadays, rising demands for improved vehicle acoustics and lower noise emissions of other components, lead to the fact that often the pump is dominant in the acoustic characteristic of hydraulic systems [3–8]. There are different ways to enhance the acoustic characteristics of a pump. One approach is e.g., to change the excitation frequencies by asymmetric spacing or to reduce the radiated noise by structural changes [3,9]. Another approach is to directly reduce the noise sources in the flow of the pump. In general, to reduce the noise radiation of a pump, a fundamental knowledge of the noise source mechanisms and the system dynamic behavior is mandatory [10–12]. To identify the source mechanisms of noise in the flow of the pump, a coupled CFD-FEM approach is chosen. The pump investigated in this work is a Bosch rotary vane pump for transmission applications with a displacement volume of 11.1 cm^3/rev. The external dimension of the housing are 70 mm in axial direction with a diameter of 110 mm. This rotary vane pump is pictured

in Figure 1. In this figure, the suction port (left picture blue part) and the delivery port (left picture red part) are spatially separated. Fluid is conveyed from the suction port, through the inlet (1) and the injector (2), to the delivery port and the outlet (3) by a set of pressure sealed displacement chambers (7). These chambers are formed by the static cam ring part (A), the static inner pump surfaces, the rotating rotor (B) and by the vanes (C), which are able to slide in and out of the rotor in radial direction. These components are pictured in Figure 1 on the right. The kinematics of the vanes is determined by the shape of the cam ring. The back vane notch (6) which is connected to the high pressure section ensures that the vanes slide along the cam ring. During the suction process the volume of a displacement chamber is increasing which leads to an inflow in the displacement chamber at the suction ports (4). Subsequently, the displacement chamber disconnects from the suction port and hence, is neither connected to the suction nor to the delivery port (5). In this phase, the volume of the displacement chamber decreases slightly, leading to a pressure rise in the displacement chamber. This so called pre-compression is already enhancing the pressure level and therefore reduces the pressure surges arising from the connection of a displacement chamber with low pressure to the delivery port with high pressure. Additionally, to ensure a smoother transition, grooves are implemented at the delivery port. These grooves connect the delivery port and the next displacement chamber, leading to a smoother volume change and hence, help to avoid high pressure surges. The optimal size and shape of these grooves is depending on the density and viscosity of the oil and the actual operating speed of the pump [13]. If the displacement chamber passes the groove and fully connects to the delivery port, the vane slides further back into the rotor. This decreases the volume of the displacement chamber leading to a fluid flow out of the chamber. The investigated pump is an asymmetric vane pump with two suction and two delivery ports. The stroke of the pump is slightly different for both delivery ports. Therefore, the pump can provide two different flow rates. The suction and delivery ports are located transversely and lead to a partly compensation of flow forces. Nevertheless, this working principle leads to flow and pressure pulsations, which excite enclosing structural elements and cause noise radiation of the pump [7,14,15]. A combined CFD-FEM approach is applied to identify which flow induced effects are crucial for the noise radiation of the pump. There are a couple of studies focusing on noise radiation of pumps. In Ref. [16] the authors investigate the fluid-borne sound of an axial piston pump by the use of a coupled 1D-3D simulation approach. The flow is modeled in a 1D simulation in AmeSim and a 3D FEM/BEM model in Virtual.Lab is used to predict noise sources and transmission paths. A similar approach is used by [8,11,12,15]. Here, the noise radiation of a gear pump is simulated using a lumped parameter model along with an FEM/BEM model. The coupling of a 3D-CFD model and an FEM/BEM model to predict the flow induced pressure pulsations and vibrations of a centrifugal pump is assessed in [17,18]. For rotary vane pumps a study using a coupled approach to analyze the structural forces acting on the rotor and vanes is presented by [19] using a 3D CFD simulation of the flow in Ansys Fluent along with Ansys Mechanical. However, there is no study to predict the fluid induced vibrations and noise radiation of a rotary vane pump using a 3D-CFD model in combination with a FEM/BEM-based model.

For this purpose, in this work the flow in the pump is analyzed using a 3D-CFD simulation model build up in the commercial software STAR-CCM+. The results of this CFD model have been validated against displacement chamber pressure measurements in [20]. Based on these results, the present paper focuses on the data transfer between the simulations and the vibroacoustic analysis. Therefore, the pressure field of this CFD simulation is mapped to a FEM grid. The pressure field is chosen, because it is assumed to be the main source in the flow for the pump's noise radiation. Subsequently, the data transfer and processing are investigated and a vibroacoustic simulation is performed in the frequency domain. The vibroacoustic simulation results are compared to acceleration and sound pressure level measurements of the pump, which have been performed in a hemi-anechoic room.

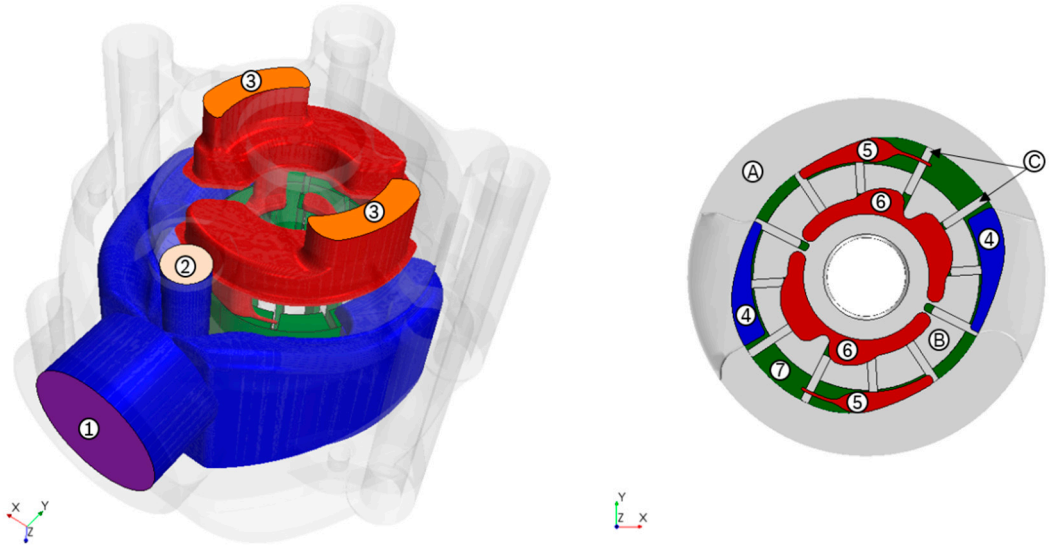

Figure 1. Rotary vane pump; (1) Inlet, (2) Injector, (3) Outlets, (4) Connection suction port to cam ring, (5) Connection delivery port to cam ring, (6) Back vane notch, (7) Displacement chamber; (A) Cam ring, (B) Rotor, (C) Vanes.

2. Methods

2.1. CFD Setup

In the present work, the model of [20] is used to perform the CFD simulations. This model uses a morphing mesh approach to discretize the moving parts. To ensure a good mesh quality a remeshing approach is applied. The unsteady Reynolds-averaged Navier-Stokes (URANS) equations are used to model the unsteady flow together with the k-ε-turbulence model. In a first step, only operating points at low rotational speeds are investigated and hence, the flow is assumed to be incompressible. For the CFD mesh a fixed angular resolution of $\Delta\gamma = 0.5°$ is chosen. Subsequently, the time step Δt is determined by the rotational speed n and the angular resolution according to Equation (5). During the CFD simulation, the pressure field acting on the static inner surfaces of the pump, which encase the flow, is written to a CGNS file in every time step. Subsequently, the pressure field is imposed as load condition in the FEM simulation. This is analogously done with the wall shear stress. Since the rotating pump surfaces cannot be modeled in a frequency response analysis, the pressure acting on the moving surfaces is used to calculate a rotor torque, which is also used as load for the FEM simulation. In this CFD model only the pump is considered. The hydraulic circuit of the transmission system or in this case of the test bench as well as resulting reflections in connected tubes are neglected.

2.2. FEM and Vibroacoustic Setup

The FEM model is build up in the commercial software Simcenter 3D (Siemens, Plano, TX, USA). As in the CFD model, only the pump is modeled, neglecting the test bench or connected tubes. The mesh of the structure consists of ten-node tetrahedral elements with a base size of 3 mm. The size and element type were estimated in a grid convergence study. The material information for the density, the Young's modulus and the Poisson's ratio is obtained from literature or data sheets and is listed in Table 1.

In Figure 2a the boundary conditions of the FEM model are displayed. The pump is fixed at six surfaces, where the screws are applied at the test bench, with fixation constraints (1). Either the part contacts in the pump are modeled by using glue or by using a contact mesh. The pump shaft is glued to the housing at the bearing positions (2). If surface to surface gluing is used, the displacements and loads are directly transferred at a mesh interface from one mesh to another. The grid points do not need to be coincident on glued surfaces [21]. The bolts connecting the housing and the cover are modeled using

beam elements with rigid spider connections (3). Similar to the experiments the acceleration is observed at the positions of the accelerometers (4.1) and (4.2) at the test bench.

Table 1. Material properties.

Parts	Material	Density [kg/m^3]	Young's Modulus [MPa]	Poisson's Ratio [-]
Housing, Cover	Pressure die-casted Aluminum	2700	74,000	0.35
Screws, Pins	Steel	7850	193,000	0.284
Cam ring	Sintered steel	6700	130,000	0.3
Shaft	Hardened steel	7850	210,000	0.3

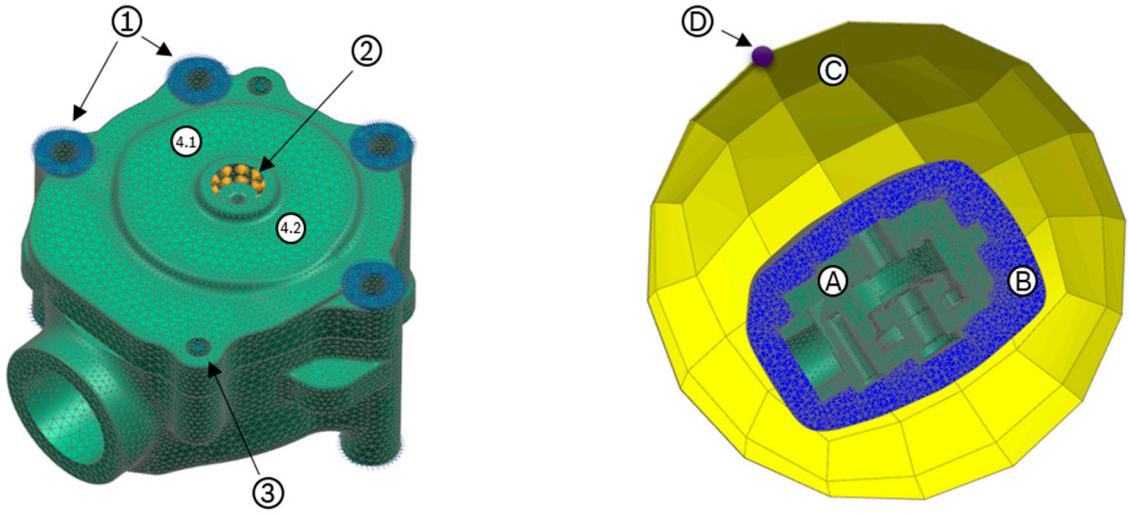

(**a**) (**b**)

Figure 2. (**a**) FEM setup (1) Fixation constraints at test bench connections, (2) Glue at shaft bearing, (3) Bolts modeled as beam elements, (4.1) and (4.2) Accelerometer positions; (**b**) Vibroacoustic setup (A) Structural mesh, (B) Acoustic fluid mesh, (C) Microphone mesh, (D) Microphone point.

In Figure 2b the meshes for the vibroacoustic model are displayed. The boundary conditions and the structural mesh (A) in the vibroacoustic model are similar to the ones of the structural model. Only the pump shaft and the gluing at the bearing positions is neglected in the vibroacoustic setup. This is justified by the investigations in Section 3.3.

In the simulation model the acoustic fluid is applied as a convex hull, which surrounds the pump. The used meshing elements are four-node linear acoustic tetrahedrons. The mesh has an extend of $\Delta\alpha = 15$ mm (Figure 2b (B)) and an element size of $\Delta\beta = 3$ mm. The size of the elements $\Delta\beta$ is estimated by the speed of sound in air $c = 343$ m/s and the maximum frequency $f_{max} = 6000$ Hz investigated in this model (see Equation (1)). Therefore, at least five elements are used per wave length (Equation (2)):

$$\Delta\beta \leq \frac{c}{f_{max}} \tag{1}$$

$$\Delta\alpha = N_e * \Delta\beta, \tag{2}$$

Here, N_e is the number of elements per wavelength. On the outer surface of the convex mesh an automatically matched layer with five layers is applied. The layers absorb all radiated sound waves providing a non-reflecting boundary condition. To compute the solution at microphone points outside the acoustic fluid mesh, the pressure and velocity at the automatically matched layer along with a boundary element method are used [21].

The sound pressure at a distance of 96 mm to the model is subsequently monitored using a microphone mesh (see Figure 2b (D)).

To obtain the loads from the CFD simulation a *Load Recipe* is used in Simcenter 3D. It uses the CGNS files from the CFD simulation as input to map the transient data of the CFD mesh to the FEM mesh. For this purpose, the CFD mesh and the pressure field or other variables of the flow can be derived from the CGNS files in Simcenter 3D. In this step, different mapping methods are available and mapping parameters need to be adjusted. Additionally, the time to frequency conversion in form of an FFT and the pressure to force conversion can be performed in this step by Simcenter 3D. For the time to frequency conversion the Hanning window is applied with the correction mode amplitude. Subsequently, the mapping process is conducted and the force amplitudes as well as their phase derived from the pressure field of the CFD simulation are available as load on the FEM grid. Because the mapping process will be investigated in this work the mapping method is explained in the following in more detail.

In Simcenter 3D there are two different mapping algorithms available. One is called *Maximum Distance* (MD), the other one *Conservative Maximum Distance* (CMD). Both methods use two mapping parameters (see Figure 3). The Maximum Distance parameter defines the search radius and the Number of Influencing Nodes parameter the number of nodes which are considered for the mapping process within the search radius.

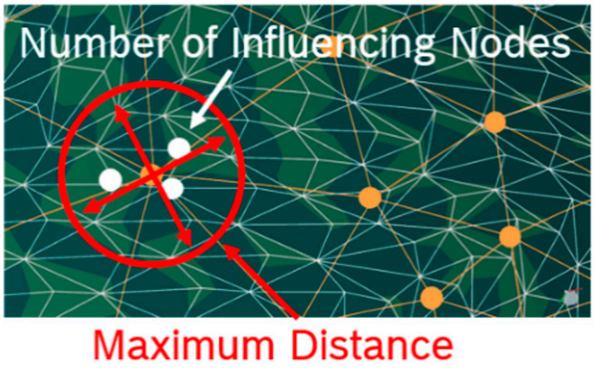

Figure 3. Mapping parameters.

In this work, the MD method is used. The MD method loops over all the target mesh nodes (FEM-Nodes) and searches within a user defined search radius (Maximum Distance) for nodes of the source mesh (CFD-mesh). Subsequently, the user defined number of nodes (Number of Influencing Nodes) of the source mesh within this search range is considered to contribute to the target mesh node and the variable is interpolated (distance weighted) to the node of the target mesh (see Figure 4).

Figure 4. Maximum distance mapping scheme.

Therefore, the MD method can consider source nodes of the CFD mesh multiple times, if the mapping parameters are not adjusted correctly. This can lead to an error due to the mapping and hence, the mapping process needs to be validated.

3. Results

In this section the mapping process is checked for validity. A further investigation focuses on the required length of the time signal and the required time step size of the CFD simulation to get an appropriate frequency resolution of the excitation forces. Additionally, a force analysis and a structural FEM simulation are performed to identify which flow phenomenon contributes the most to the excitation of the pump housing. Finally, a vibroacoustic simulation is preformed using the parameters from the previous investigations and its results are compared to acceleration and sound pressure level measurements performed in a hemi-anechoic room.

3.1. Mapping Validation

In order to ensure, that the source for the excitation is correctly transferred from the CFD to the FEM mesh a criterion is needed to check the original and the mapped data. For this purpose, it is decided to use the sum of the forces caused by the flow as a criterion. Since, the surface on which the pressure is acting on in the CFD and the FEM simulation remains the same, the force sum has to be equal in both models:

$$F = \int pdA, \tag{3}$$

To determine this excitation force F caused by the static pressure p, the surface integral of the pressure acting on the enclosing pump surfaces A is evaluated (Equation (3)) in the CFD simulation. In a first step, only one time step of the CFD simulation is taken into account. The pressure acting on the rotating parts of the pump is excluded from the mapping process, because moving meshes can not be used in the frequency response analysis in the FEM simulation. Subsequently, the mapping action of the fluid pressure from the CFD to the FEM grid is performed and the resulting forces are calculated in Simcenter 3D. The sum of these resulting forces is evaluated in the FEM model. To verify that the pressure is transmitted correctly to the FEM mesh and to estimate the size of the error, the force sum of the original CFD data and the force sum after the mapping action are compared. Furthermore, the mapping result is checked by comparing the CFD and the FEM pressure distribution visually. At first, the influence of different mapping parameters on the mapping result is investigated. In the following investigations the base size of the CFD mesh (source mesh) is 1 mm and the base size of the FEM mesh (target mesh) is set to 3 mm using ten-node tetrahedral elements.

In this investigation the parameter Number of Influencing Nodes is set to 4, while the Maximum Distance parameter is varied. In Figure 5 it is visible that the maximum distance parameter has a high impact on the mapping result. In an initial guess, the maximum search distance is set to 0.75 mm, because ten-node tetrahedral elements of a base size of 3 mm are used. That means the half node distance between two target mesh (FEM mesh) nodes is used as search distance. As can be seen from Figure 5, this guess seems to be valid. As the maximum search distance is enhanced, the force sum in the FEM simulation is increased nearly linear, leading to higher, physically incorrect force values. If the maximum search distance is decreased, the force sum in the FEM simulation drops below the force sum of the CFD simulation indicating a loss of information. As a consequence, the search distance is set to 0.75 mm for all further investigations.

To investigate the influence of the parameter Number of Influencing Nodes, the maximum search distance is held constant at 0.75 mm. Figure 6 shows, that the impact of the parameter Number of Influencing Nodes on the mapped force sum is less significant, than the maximum search distance. For a number of three nodes, the force sum in the mapped data shows a minimum, while the total force sum is still overprediced by about 30 N. Therefore, a number of three influencing nodes are chosen for all further investigations. Furthermore, this can be justified by the fact, that a 3D surface is used and one node is considered for each spatial direction.

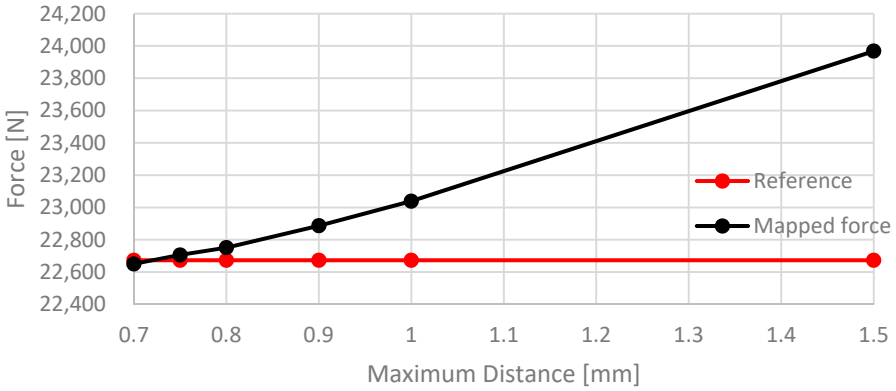

Figure 5. Influence of the maximum distance parameter on the mapped force sum.

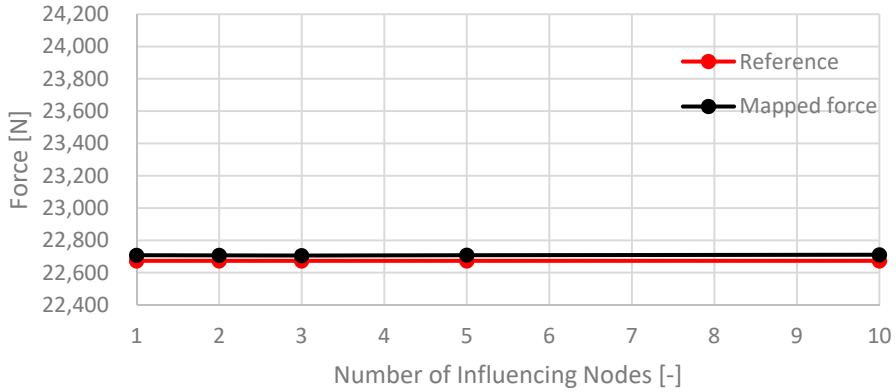

Figure 6. Influence of the number of influencing nodes parameter on the mapped force sum.

For the estimated mapping parameters, the total error for the mapping process at this time step is 0.144%. In the next steps the influence of different mesh sizes of target mesh and source mesh on the mapping error should be investigated. At first the source mesh size (CFD mesh) is varied. The results can be seen in Figure 7.

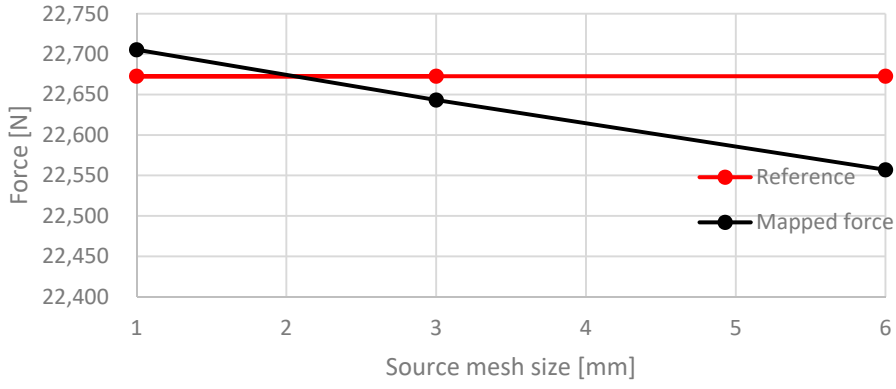

Figure 7. Influence of the source mesh size on the mapped force sum.

It is clearly visible, that a larger source mesh size leads to a loss of information and hence, the force sum drops below the reference force derived from the original CFD mesh, if the mapping parameters are held constant. This is caused by the lower number of source mesh nodes within the search distance of the target mesh. That means some target mesh nodes, which should have a load are not able to find a corresponding source mesh node within the search distance. This effect is vice versa for smaller source meshes. Some nodes, which should not have a load are able to find a source mesh node within the search radius. Consequently, the force sum transmitted to the target mesh increases, because source nodes

are considered multiple times for the mapping process. The influence of the target mesh size can be seen in Figure 8.

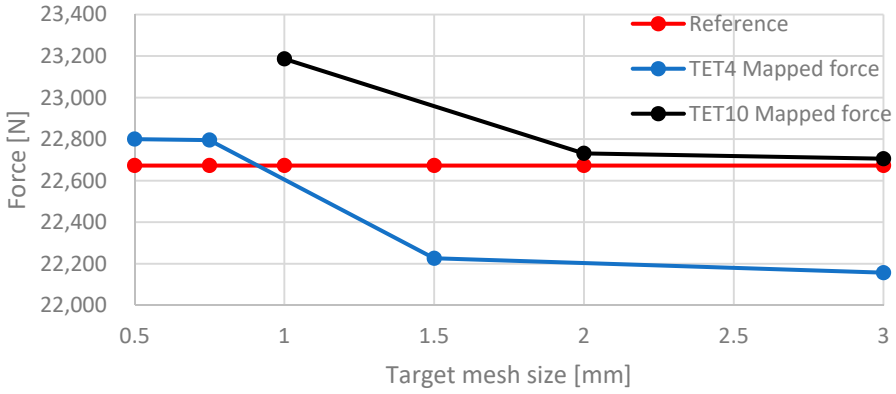

Figure 8. Influence of the target mesh size on the mapped force sum.

The mapping parameters have been adjusted for the ten-node tetrahedral elements mesh with a base size of 3 mm. Figure 8 shows, that the mapping error increases for all other target mesh sizes. On one hand, this is related to the MD method. Since, the adjusted maximum search distance is chosen for a ten-node tetrahedral elements mesh with a base size mesh of 3 mm the maximum search distance for other meshes is not optimal. On the other hand, it is expected, that a four-node tetrahedral elements mesh with a base size of 1.5 mm shows similar results as the reference mesh, because the initial guess for the half node search distance is 0.75 mm in this case, too. It is not clear, why the error is higher in this case. Overall, the target mesh size has a high impact on the mapping error and hence, the mapping parameters have to be adjusted for the derived mesh sizes.

In a last step the impact of different transient conditions on the mapping error are evaluated. The results are pictured in Figure 9. This is done, because the CFD simulation uses a morphing mesh method, which could lead to a different node distribution in every time step. Additionally, this check allows to draw conclusions regarding the mapping procedure. If the force sum of the CFD simulation drops at any point below the force sum of the FEM simulation, this could hint towards neglected source nodes during the mapping procedure.

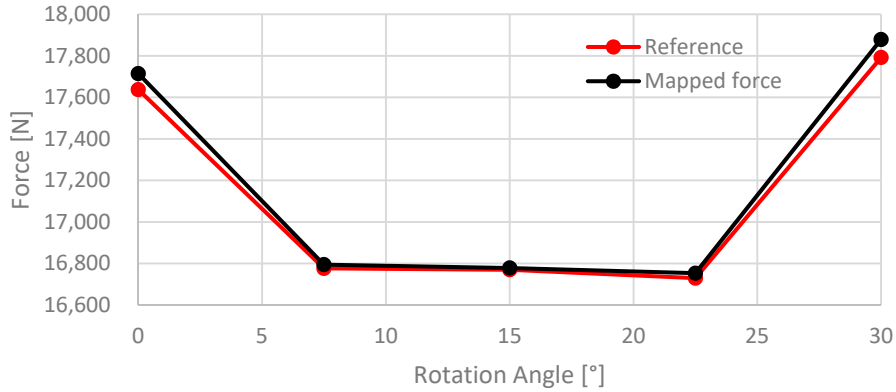

Figure 9. Influence of morphing mesh nodes on the mapped force sum.

From Figure 9 it is visible, that the mapping error depends on the actual angular position of the pump rotor. While at a rotation angle around 0° and 30° the mapping error is higher (at about 0.5%), the mapping errors for 7.5°, 15° and 22.5° are lower (at about 0.1%). This could be traced back to pressure surges occurring at 0° and 30° in the CFD model (also visible by the higher force sum). These pressure surges are tracked in a high number of small computational cells, which could lead to an overprediction in the FEM

model, if mesh nodes of these cells are considered multiple times during the mapping action. However, the overall mapping error is still less than 0.5% and consequently, the mapping procedure does not significantly affect the results.

3.2. Required Time Signal

In the CFD simulation a transient solution in the time domain is obtained, while in the FEM simulation the solution is obtained in the frequency domain. In order to prescribe dynamic loads in the FEM based on the CFD results, a Fourier transformation of the time evolution of the pressure in the flow field through the pump is necessary. In the present work, this is realized in Simcenter 3D. In order to obtain an appropriate excitation signal from the transient evolution of the pressure field, the time step as well as the length of the time signal are important. The time step determines the highest frequency which can be resolved. The length of the time signal determines the lowest frequency which can be resolved as well as the increment Δf for a given time step. A longer time signal leads to a better frequency resolution, but also the computational effort increases. This investigation focuses on the length of the time signal and the resulting forces of the signals in the frequency domain.

The sampling frequency is the reciprocal of the time step and determines the maximum resolvable frequency by the means of the Nyquist-Shannon sampling theorem. The Nyquist-Shannon sampling theorem states, that the maximum frequency f_{max} of a signal, which can be obtained is half of the sampling frequency f_s, i.e.,:

$$f_{max} \leq \frac{f_s}{2} \,. \tag{4}$$

In the CFD simulation a fixed angular resolution of $\Delta\gamma = 0.5^\circ$ is applied, which gives the time step depending on the actual rotational speed n (Equation (5)). Since in the present approach each time step is used to process the dynamic loads this equals the inverse of the sampling frequency,

$$\Delta t = \frac{1}{f_s} = \frac{\Delta\gamma}{360^\circ * n} \,. \tag{5}$$

The frequency resolution of the signal is obtained from the interval size of the signal. If the solution is stored each time step, then N_s data files are written during one revolution, i.e.,:

$$N_s = \frac{360^\circ}{\Delta\gamma}. \tag{6}$$

This leads to N_b bins which are available to process the FFT for N_{rev} pump revolutions:

$$N_b = N_{rev}\frac{N_s}{2} \tag{7}$$

The increment Δf in the frequency domain is calculated by Equation (8):

$$\Delta f = \frac{f_{max}}{N_b} = \frac{n}{N_{rev}} \tag{8}$$

Subsequently, the number of pump revolutions used for the time signal processing and the rotational speed of the pump determine the resolution of the time signal in the frequency domain. This is caused by the fixed time step of the CFD simulation which is depending on the rotational pump speed and is determining the sampling frequency f_s. The only way to adjust the frequency resolution in this case is to use a different time signal length for the time to frequency conversion. Therefore, the number of revolutions N_{rev} influences the maximum forces obtained from the time evolution of the pressure field at different frequencies due to the changing frequency resolution.In the transient simulation of the pump, the characteristic flow phenomena repeat every 30°, because the investigated

pump has $N_v = 12$ vanes. The blade passing frequencies $f_{bp,k}$ and its kth-harmonics are defined in Equation (9):

$$f_{bp,k} = k * N_v * n, \quad k = 1, 2, 3, \ldots \tag{9}$$

The minimum number of revolutions, which can be used for the time to frequency conversion, is $N_{rev} = 1/12$ pump revolution. Note that the CFD simulation has to be already at a steady state condition, when the pressure field is stored. The obtained forces for 30°, 90°, 180°, 360°, 720°, 1440° and 2160° rotation angle of the pump are investigated for a rotational speed of 2000 rpm (see Table 2). The time step size is 4.16E-05 s for all simulations and the maximum resolvable frequency f_{max} derived by Equation (4) is 12,000 Hz. The results are pictured in Figure 10.

Table 2. Frequency resolution depending on number of revolutions at 2000 rpm.

Rotation Angle [°]	N_{rev} [-]	Δf [Hz]
30	1/12	400
90	1/4	133.3333
180	1/2	66.6667
360	1	33.3333
720	2	16.6667
1440	4	8.3333
2160	6	5.5556

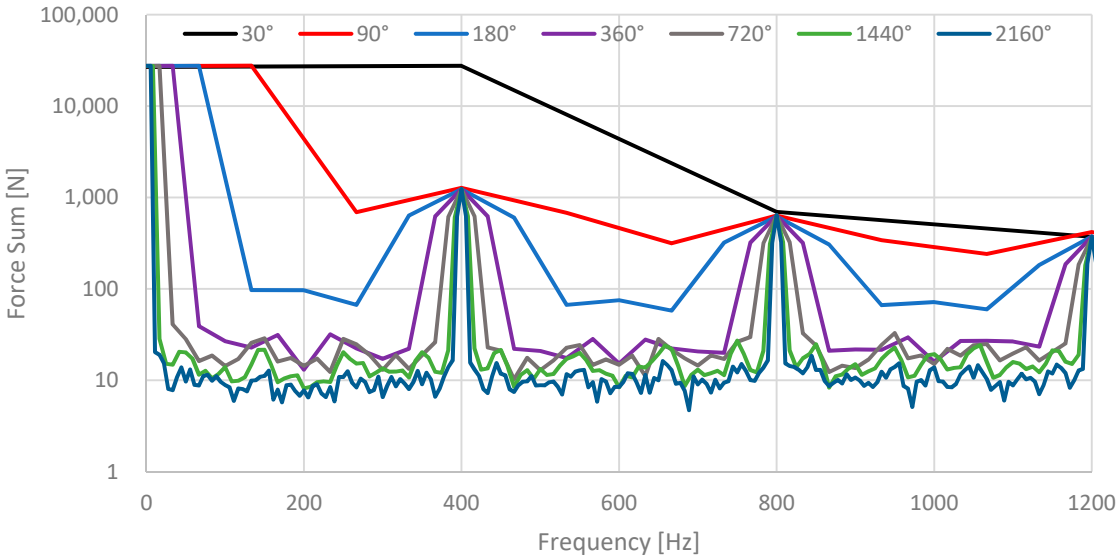

Figure 10. Influence of time signal length on the forcing frequencies at 2000 rpm.

The blade passing frequency of the pump and two harmonics are visible at 400 Hz, 800 Hz and 1200 Hz. At the blade passing frequency (400 Hz) it is visible that the excitation force obtained from 30° revolution of the pump is higher than in the other cases. This is due to the smallest resolvable frequency in this case which is 400 Hz and consequently, the forces of the static pressure are obtained at this frequency due to the low frequency resolution. In all other cases, the amplitudes of the excitation forces show nearly similar amplitudes at the blade passing frequency and its harmonics. The excitation forces at intermediate frequencies (between the blade passing frequency and its harmonics) are overpredicted for the 90°-case and the 180°-case due to the low frequency resolution. Here, the side lobe response of the blade passing frequency and its harmonics overpower the main lobe responses of nearby week sinusoidal signals. For the cases using more than one pump revolution, the increasing number of samples leads to an increased frequency

resolution and to a narrowing of the lobes at the blade passing frequency and its harmonics. Consequently, the ability to distinguish between two closely spaced frequency components increases, leading to overall lower amplitudes. Especially, near the blade passing frequency and its harmonics as well as at the intermediate frequencies the magnitude of the obtained excitation forces reduces with an increased frequency resolution.

From Figure 11 it can be seen that the locations of high excitation forces at a frequency of 400 Hz are the same for 90°, 180° and 360° time signal length. For 30° the location is different and the excitation is not captured correctly. If only transient data of 30° are used as excitation force, the complete delivery port shows high excitation forces due to the low frequency resolution and the influence of the 0 Hz lobe. For 90°, 180° and 360° transient data the excitation forces are only visible in the area in which the displacement chamber disconnects from or connects to the delivery port. This is caused by the pressure change, which appears with the blade passing frequency of 400 Hz at a pump speed of 2000 rpm.

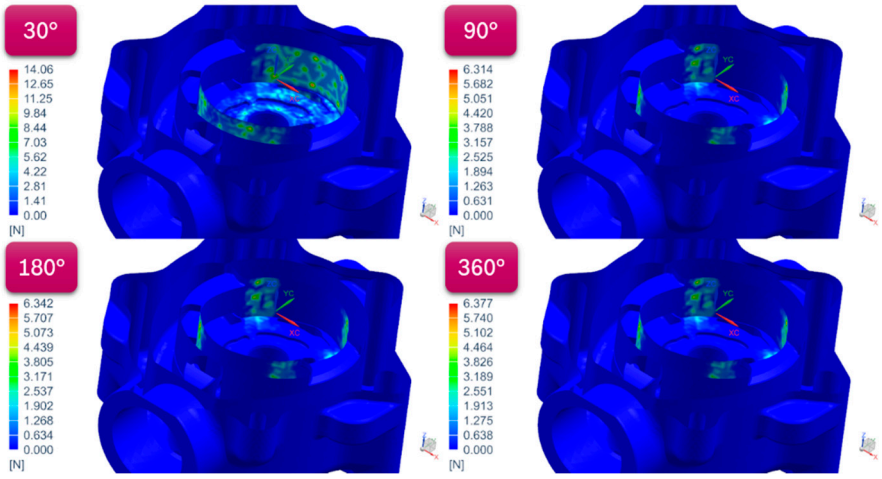

Figure 11. Force distribution in the FEM model at 400 Hz.

To achieve a tradeoff between simulation time and frequency resolution, it is decided, that transient files of one revolution (360°) are used to obtain the excitation forces of the pump for the FEM simulation. The blade passing frequency of the pump and its harmonics are captured well and the amplitudes of frequencies between the blade passing frequency and its harmonics are already in the same order of magnitude as with more pump revolutions. Consequently, all effects occurring during one revolution of the pump are captured in the excitation forces.

Table 3 shows the time step size of the CFD simulation, the maximum resolvable frequencies of the signal and the frequency resolution for different investigated rotational speeds for one pump revolution. Note that the time step has to be chosen carefully in order to achieve a reasonable convergence in the CFD simulation.

Table 3. Relations between operating points, time and frequency resolution.

Rotation Rate [rpm]	Δt [s]	N_s [-]	f_s [Hz]	N_b [-]	f_{max} [Hz]	Δf [Hz]
1000	8.3333×10^{-5}	720	12,000	360	6000	16.6667
1500	5.5555×10^{-5}	720	18,000	360	9000	25.0
2000	4.1667×10^{-5}	720	24,000	360	12,000	33.3333

From Table 3 it is clearly visible, that a smaller time step and consequently, a higher sampling frequency leads to a lower frequency resolution Δf, for the same number of revolutions. On the one hand, with the applied time step size of the CFD simulation for the 1000 rpm simulation, excitation frequencies are only resolvable up to 6000 Hz. On the other hand, the frequency resolution of the data for the 2000 rpm CFD simulation

is rather coarse (33.3333 Hz). This effect has to be taken into account and leads to the fact that at higher rotational speeds the number of pump revolutions used for the time signal processing needs to be increased to get the same time signal length and a reasonable frequency resolution of the signal. The influence of a higher frequency resolution on the vibroacoustic solution is derived in Section 3.4.

3.3. Influence of Fluid Rotor Forces and Wall Shear Stress

In the FEM simulation the solution is computed in the frequency domain. Hence, it is not possible to model the rotating surfaces of the rotor and the vanes (see Figure 1B,C) in the FEM setup. Consequently, the fluid forces in form of pressure and wall shear stress acting on these rotating surfaces cannot be transferred to the FEM grid. Therefore, it is decided to estimate the contribution of these fluid rotor forces (FRF) to the excitation of the pump housing in form of a rotor torque. This torque is implemented in the FEM simulation at the mid position of the rotor in the shaft. Furthermore, the magnitude of the forces resulting from the pressure and the wall shear stress acting on the static flow enclosing pump surfaces (FEPS) is investigated, too. These surfaces include the blue and red surfaces in Figure 1 left and in Figure 1 right the inner surface of the cam ring (A).

To get a first order of magnitude of the FRF, the resulting forces due to the pressure field and the wall shear stress are evaluated on the rotating parts in the CFD simulation. Because the investigated pump is a double stroke type vane pump, the FRF can compensate each other, due to the transversally located high pressure and low pressure sections (see Figure 1). Therefore, the resulting fluid force acting on the rotor parts, which can lead to a deflection of the rotating parts, is of interest for the excitation of the pump housing. For this purpose, the resulting FRF in each spatial direction are calculated. Then the magnitude of the three force vectors is determined.

Table 4 shows the time averaged value of the resulting forces in the transient CFD simulation and the fluctuation of these forces in form of its standard deviation. The resulting forces are derived one time considering the static pressure acting on the FEPS, one time considering the wall shear stress acting on the FEPS and one time for the FRF. These values are evaluated at three different operating points. It is visible, that the FRF show low resulting standard deviations and low resulting mean values compared to the pressure field acting on the FEPS for all operating points. This can be explained by the methodology, where all the forces in each direction are summed up, before comparing the forces. Nevertheless, it is possible to compare the forces using this methodology, because most FRF act against the direction of rotation of the pump and the shaft has a rotational degree of freedom. Therefore, mainly the resulting forces, which lead to a deflection of the shaft from its initial position, will contribute to the pump's noise radiation via the pump housing. As it can be seen in Table 4, the resulting average FRF as well as the resulting average force from the wall shear stress acting on the FEPS is about three orders of magnitude lower than the forces resulting from the static pressure acting on the FEPS. In addition, the standard deviation which represents an evaluation criteria for the force fluctuations is less significant for the wall shear stress acting on the FEPS and for the FRF.

Table 4. Force fluctuations at different operating points.

Operating Point	Value	Pressure on FEPS	Wall Shear Stress on FEPS	FRF
2000 rpm, 15 bar	Average [N]	1.69×10^4	3.53×10^0	2.99×10^1
	Standard deviation [N]	2.15×10^2	9.76×10^{-2}	7.72×10^0
1000 rpm, 15 bar	Average [N]	1.66×10^4	2.33×10^0	2.53×10^1
	Standard deviation [N]	6.10×10^1	5.01×10^{-2}	6.85×10^0
2000 rpm, 10 bar	Average [N]	1.16×10^4	2.94×10^0	2.59×10^1
	Standard deviation [N]	2.68×10^2	1.30×10^{-1}	1.06×10^1

Consequently, the forces and force fluctuations resulting from the wall shear stress acting on the FEPS and the FRF are less significant for the pump's noise radiation than the forces caused by the static pressure acting on the FEPS at the investigated operating points. The magnitude of the wall shear stress force acting on the FEPS is even lower than the error of 0.5% due to the data mapping compared to the static pressure acting on the FEPS. Therefore, the wall shear stress will be neglected in the following investigations. The influence of the FRF is investigated further by the use of a structural model.

Figure 12 displays the acting forces on the pump housing resulting from the static pressure acting on the FEPS at different operating conditions. The resulting forces are pictured at the blade passing frequency for 2000 rpm and 15 bar (a) and for 1000 rpm and 15 bar (b). The locations in Figure 12, where the highest forces are tracked for the blade passing frequency match with the locations of high forces at k-times the blade passing frequency. These frequencies were chosen for evaluation, because the highest noise radiation of the pump takes usually place at the blade passing frequency and its harmonics. Regarding Figure 12a,b only small differences in the locations of high load can be observed. In the top view four locations of high load can be identified. These locations are similar for different operating points and are located between the pressure and the suction port. The spatial extend of these locations with high forces matches the angular extend of a conveying chamber of the pump (here 30°). The locations where high forces occur can be traced back to the pressure signal of the vane pump (compare Figure 18), which shows a pressure rise from about 1 bar at the suction port to the pressure level of the delivery port or vise versa at these locations. At these locations additional pressure surges may arise, if the pump is not optimized for the operating condition. This is caused by the instantaneous connection between a chamber with low pressure and the delivery port. The blade passing frequency always shows the highest force amplitudes (compare Figure 10). The magnitude of the forces at the blade passing frequency is mainly depending on the pressure difference from suction to delivery port. If the rotational speed of a pump is increased, the blade passing frequency with the highest force amplitude as well as its harmonics are shifted to higher frequencies. Therefore, the pump housing is excited at higher frequencies.

This investigation underlines that the change in the static pressure of the flow and the resulting pressure surges are the flow phenomena which contribute most to the pump's noise radiation. For sure, this is only valid for standard operating conditions of the pump. If the rotational speed is increased and exceeds the cavitation onset or air is introduced into the system, additional high pressure fluctuations and hence, non-negligible noise sources may arise in the pump [22,23].

To verify the conclusion that the FRF have less impact on the noise radiation of the pump, the excitations of the pump housing resulting from the FRF and from the static pressure acting on the FEPS are investigated. The simulations are performed using the FEM setup for the structural model described in Section 2.2. One simulation is performed only considering the FRF in form of a rotor torque and one simulation only considering the forces due to the static pressure acting on the FEPS. To estimate the magnitude of the excitation by the rotor torque, the shaft is glued to the pump housing at the bearing positions. In the real pump the axial shaft position is derived by the pressure forces in the fluid. The plain bearings are lubricated by a leakage oil connection to the conveyed oil. Therefore, the shaft can usually not handle axial forces and has only a rotational degree of freedom. Hence, the excitation through the rotor torque is exaggerated in this model. To evaluate the impact of the FRF and the pressure field acting on the FEPS, the velocity at four representative positions at the outer surface of the pump housing is analyzed and compared. The locations are pictured in Figure 13 in red. The outer surface of the pump housing is chosen, since the noise radiation outside of the pump, which excites the surrounding air, is of interest. Subsequently, an average of the surface velocity of these four locations is calculated. The average can be seen in Figure 14. The evaluated frequencies of this investigation range from 100 Hz to 1300 Hz with a step size of 100 Hz. The rotational

speed of the underlying simulation is 2000 rpm and the pressure load is 15 bar. Hence, the first blade passing frequency and two harmonics can be observed.

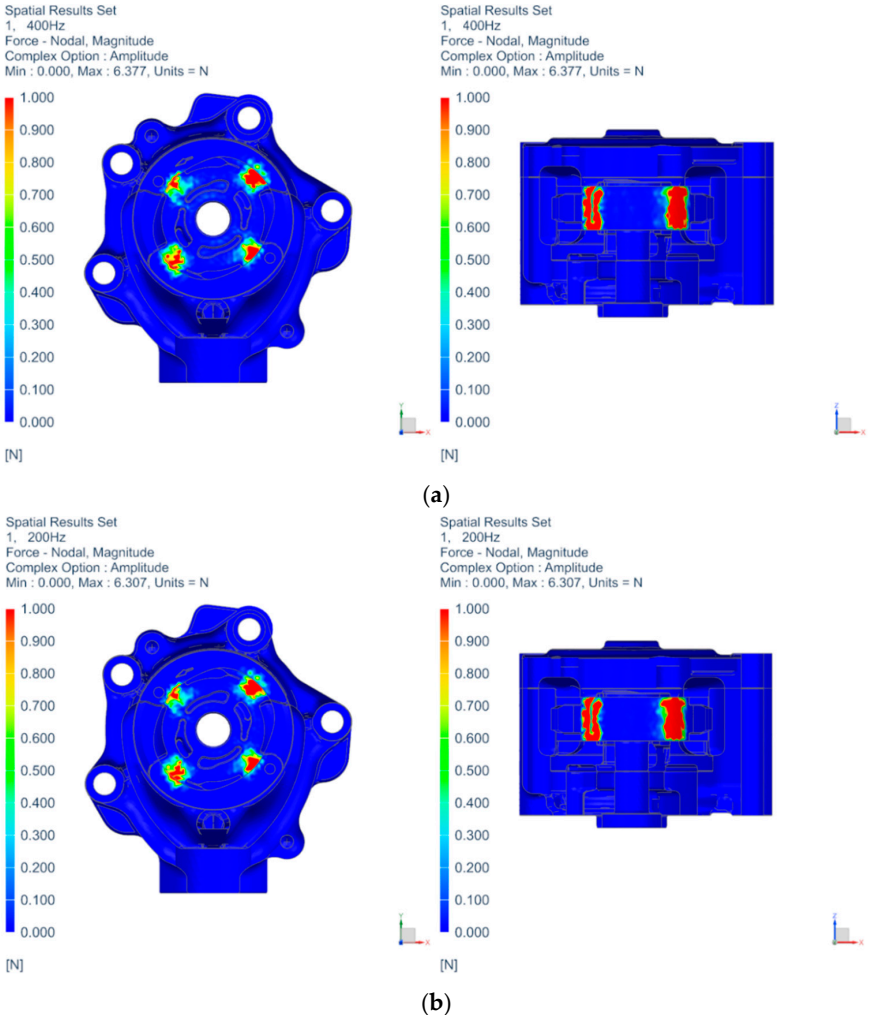

Figure 12. Locations of high excitation forces due to the static pressure in the pump housing at blade passing frequencies; (**a**) 2000 rpm and 15 bar at 400 Hz; (**b**) 1000 rpm and 15 bar at 200 Hz.

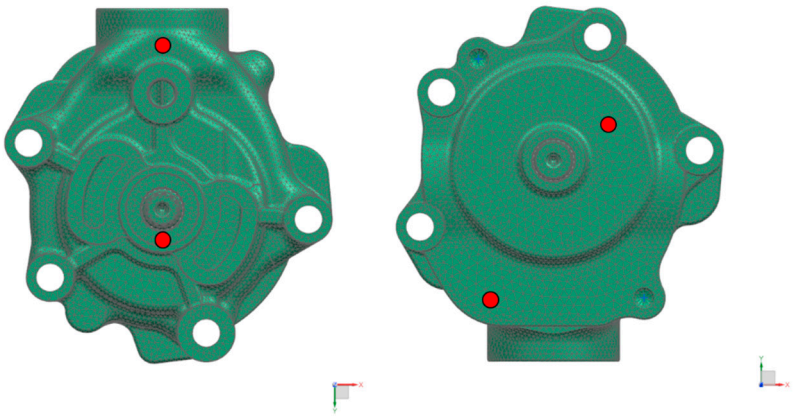

Figure 13. Positions where the surface velocity is evaluated.

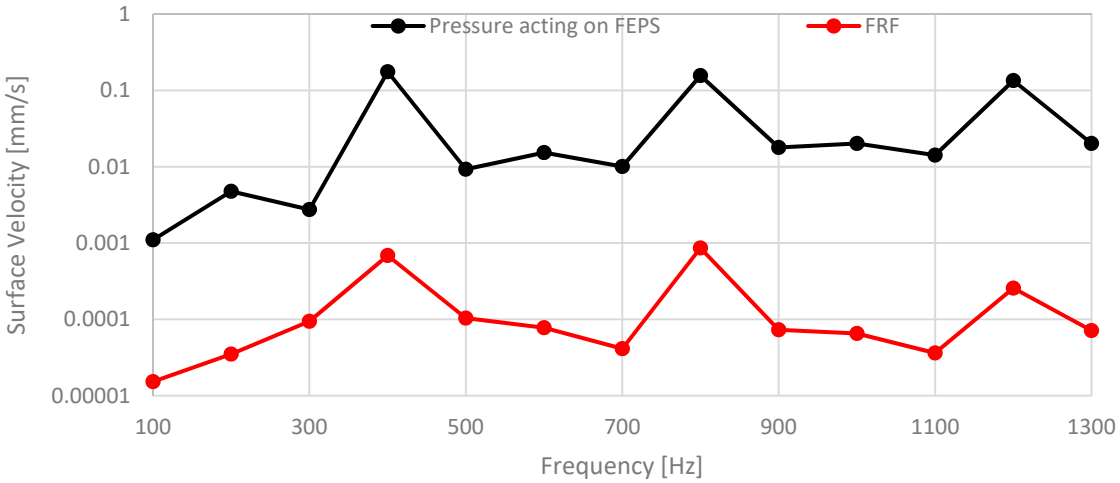

Figure 14. Comparison of the surface velocity magnitudes caused by FRF and pressure on FEPS.

It is clearly visible that the excitation on the exterior surface of the pump housing shows the same blade passing frequency and harmonics for the FRF and the pressure acting on the FEPS. These frequencies are only depending on the rotational speed and the number of displacement chambers. Furthermore, the excitation on the exterior surface of the pump housing by the FRF is about 200 times lower (logarithmic scale) than the excitation due to the pressure acting on the FEPS. Since the shaft is glued to the pump housing, the excitation of the pump housing due to the FRF caused by the flow should be overestimated in the model. That means, in the experiment the vibration of the pump housing, due to the FRF is negligible for this pump type.

This is underlined by simulations at different delivery pressures and rotational speeds, too (see Figure 15). Here, the ratio of the surface velocity caused by the FRF v_{FRF} with regard to the surface velocity caused by the pressure acting on the FEPS v_{FEPS} is visualized. For that purpose, an average value of the surface velocity at the four surface nodes of the pump housing is calculated similar to the previous investigation. Additionally, the results at the blade passing frequency and at two harmonics are averaged to achieve a representative single value (see Equation (10)):

$$R_{FRF} = \frac{\overline{v_{FRF}}}{\overline{v_{FEPS}}} \tag{10}$$

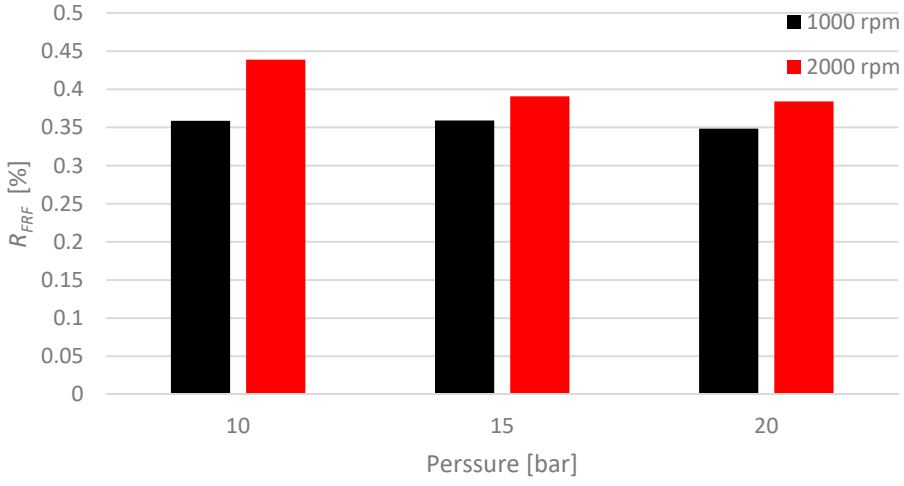

Figure 15. Comparison of R_{FRF} for two different pressure loads and rotational speeds.

Figure 15 shows that an increased rotation rate leads to slightly higher proportions of the rotor torque in the resulting surface velocity. However, the ratio is still lower than 0.5% for 2000 rpm at all loads. Because only lower rotational speeds up to 2000 rpm are investigated in this work, it is decided to neglect the rotor torque in the vibroacoustic simulations in the next section.

3.4. Vibroacoustic Results

For this investigation the vibroacoustic model as described in Section 2.2 is used. To validate the results of the vibroacoustic model the acceleration at the sensor positions and the sound pressure level at a specific microphone point in 96 mm distance to the pump surface is compared to measurements at 2000 rpm and 15 bar. The measurements are performed at an acoustic test bench in a hemi-anechoic room (see Figure 16). The powertrain of the test bench is located outside of the hemi-anechoic room to measure only the noise caused by the pump itself. However, to ensure the pump function a test device to mount the pump, as well as connections to the suction and delivery ports in form of tubes are mandatory, which are located in the hemi-anechoic room and influence the measured noise radiation.

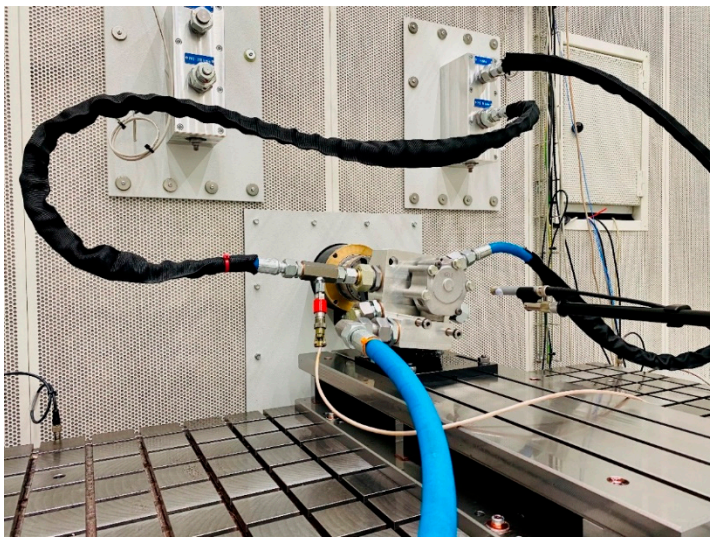

Figure 16. Sound pressure level measurement setup in a hemi-anechoic room.

The first investigation focuses on the number of revolutions of the pump needed to capture the sound pressure in the frequency domain accurately. In a pre-investigation of the excitation forces from the load, it was found that at least transient data of one revolution is required to get an appropriate resolution of the excitation forces in the frequency domain (see Section 3.2). Therefore, the impact of different numbers of transient data N_s derived by different numbers of complete revolutions of the pump are analyzed. Table 5 shows the resulting properties for the investigated numbers of revolutions.

Table 5. Parameters of the CFD simulation and the resulting properties in the frequency domain.

Number of Revolutions [-]	Rotation Rate [rpm]	Δt [s]	N_s [-]	f_{max} [Hz]	N_b [-]	f_s [Hz]	Δf [Hz]
1	2000	4.1667×10^{-5}	720	24,000	360	12,000	33.3333
2	2000	4.1667×10^{-5}	1440	24,000	720	12,000	16.6667
4	2000	4.1667×10^{-5}	2880	24,000	1440	12,000	8.3333

Figure 17 shows the results of the predicted sound pressure level at the microphone point in 96 mm distance to the pump housing for one, two and four revolutions of the pump. The solution of the FEM model is computed for each excitation frequency. It is

clearly visible that the blade passing frequency of the pump and its harmonics at k-times 400 Hz are visible in all solutions. The magnitude of at the blade passing frequency and its harmonics is nearly independent of the number of revolutions used for the excitation of the pump. Nevertheless, as the frequency resolution increases, the resulting amplitudes at the blade passing frequency and its harmonics narrow and appear over a reduced frequency range. Additionally, the fluctuations of the sound pressure level between the blade passing frequency and its harmonics increase and occasionally different trends and small deviations occur.

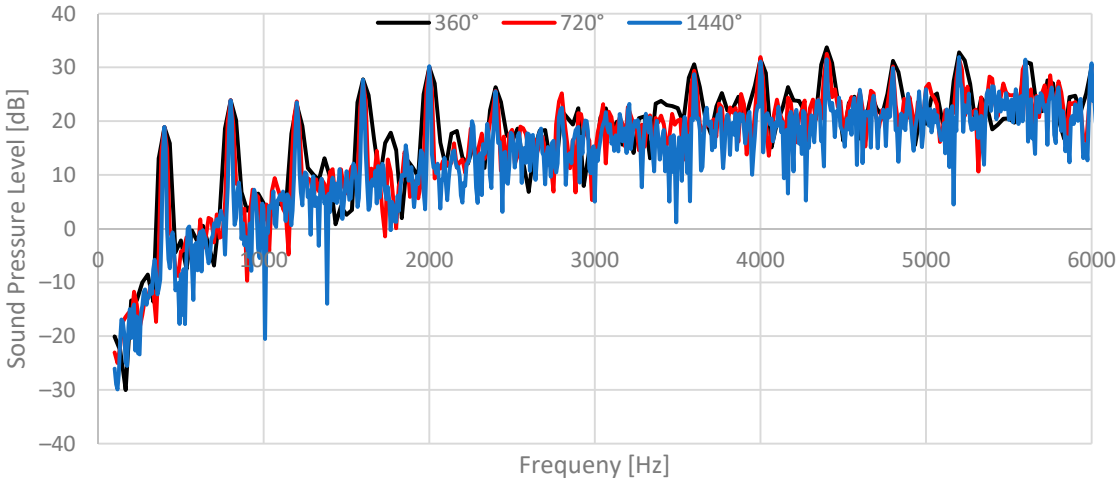

Figure 17. Sound pressure level derived by the vibroacoustic solution for different numbers of pump revolutions.

The frequencies, which match the blade passing frequency of the pump and its harmonics, usually contribute with the highest amount to the pump's noise radiation. Since, these frequencies are predicted in all simulations approximately with the same magnitude it is decided to use only one revolution of the pump to reduce the required computational time.

Subsequently, the vibroacoustic results of the surface acceleration and of the sound pressure level at the microphone point are compared to the measurements performed in the hemi-anechoic room. In order to do so, the excitation signal of the pump has to be correct. Therefore, the pressure in a displacement chamber of the pump is monitored (compare [20]). The numerical and experimental results for 2000 rpm and 15 bar outlet pressure are displayed in Figure 18.

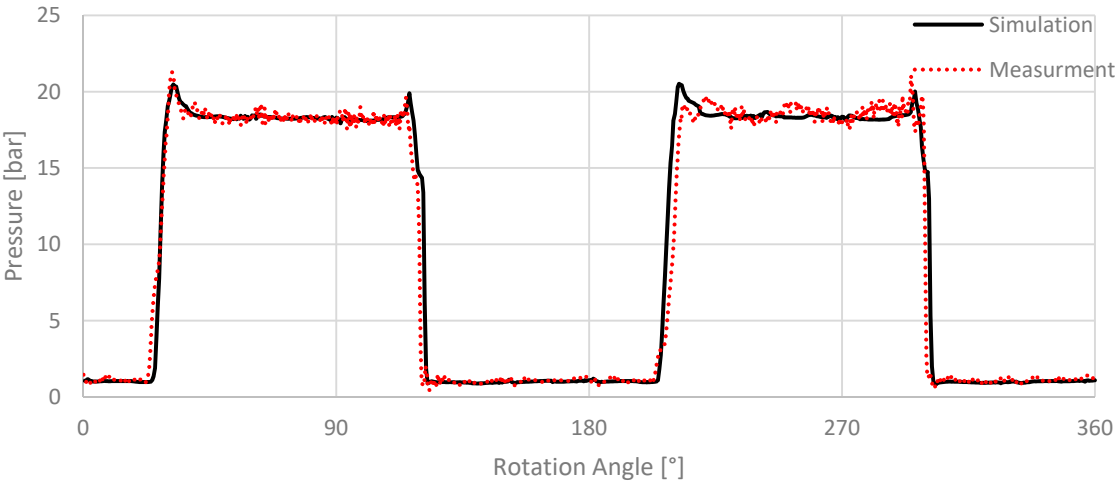

Figure 18. Internal displacement chamber pressure of simulation and measurement for 2000 rpm and 15 bar.

On the one hand it can be seen, that the characteristic pressure curve could be captured well. On the other hand, at the second delivery port some fluctuations in the high pressure section of the measurement which are not captured by the simulations are visible. These may result from interactions with the connected system. Additionally, the high frequency fluctuations visible in the measurement cannot be captured by the CFD simulations. Possible causes for these fluctuations are vibrations of the pump housing and pipes, which interact with the fluid in the pump [20]. Overall, the simulation and the measurement show a reasonable agreement.

To validate the results of the simulation model, the surface acceleration of the model and the measurement is compared for the two different sensor positions (see Figure 2a). The results are displayed in Figure 19a,b.

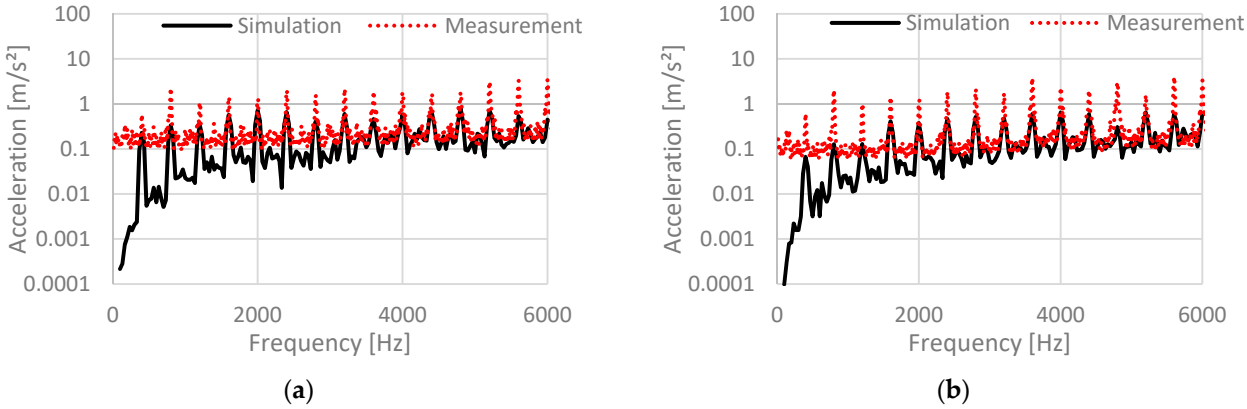

Figure 19. Surface acceleration obtained from the simulation and measurement for 2000 rpm and 15 bar; (**a**) Sensor position 4.1); (**b**) Sensor position (4.2).

These figures show that the blade passing frequency and its harmonics are clearly visible in the simulation and in the measurements. However, the simulation underpredicts the accelerations over the whole evaluated frequency range. While there is a huge deviation at low frequencies up to 2400 Hz, the agreement at higher frequencies becomes better. The accelerations at the frequencies between the blade passing frequencies are in a reasonable agreement with the measurements above 4000 Hz, while the acceleration amplitudes at the blade passing frequency and its harmonics are still underpredicted. In the next step, the sound pressure level at the microphone point is compared to the measurement. The results can be seen in Figure 20.

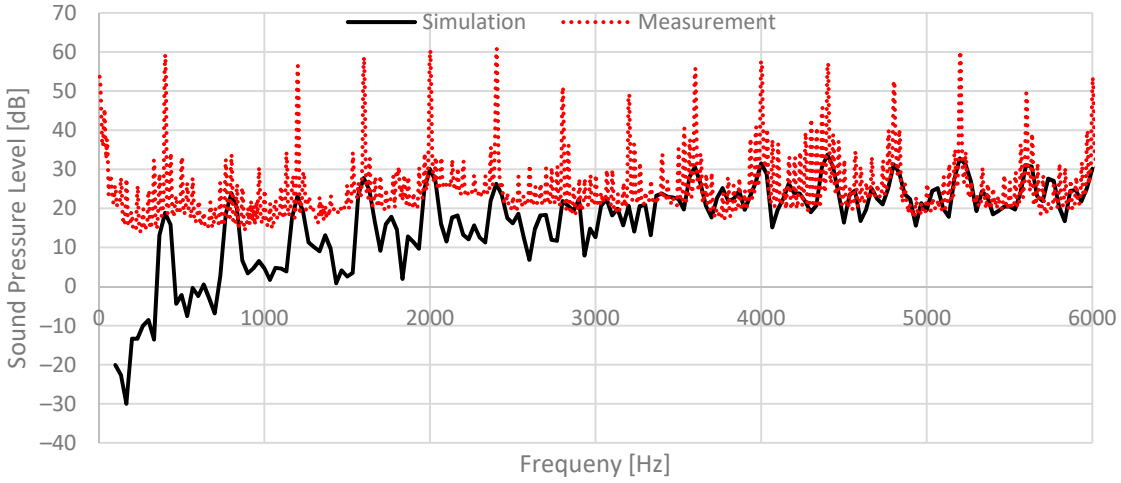

Figure 20. Sound pressure level obtained from simulation and measurement for 2000 rpm and 15 bar.

It is visible that at low frequencies the sound pressure level is underpredicted in the simulation similar to the surface accelerations. A noticeable deviation between the simulation and the experiment can be observed at the blade passing frequency and its harmonics. The peaks in the measurement are sharper than in the simulation, which is caused by the lower frequency resolution in the simulation. At about 3800 Hz to about 6000 Hz the magnitude of the sound pressure level in the simulation shows a good agreement with the experiment, even though the sound pressure level at the harmonics of the blade passing frequency is underpredicted. All harmonics of the blade passing frequency, except the ones at 2800 Hz and 3200 Hz are visible in the simulated sound pressure level. At these frequencies the measurement shows a reduction in the amplitude too. Except at low frequencies, the simulation results capture the relevant effects visible in the measurements. This is mainly caused by the simplifications used in the vibroacoustic simulation model. In this model, only the stiff pump housing is contributing to the noise radiation of the pump. Because only the pump is investigated in the model, fixation constraints at the pump housing are necessary, which lead to a less vibration-prone simulation model. In the experiment, the test device and tubes can be easier excited by the lower harmonics of the blade passing frequency of the pump than the pump housing itself and contribute to the noise radiation (see Figure 15). Especially, the pressure pulsation in the tubes connected to the pump is an additional source of vibration and noise radiation of the pump, which is not considered in this approach. Furthermore, the surfaces which can excite the surrounding air are much smaller in the simulation model. In the pump itself, additional noise sources arise from the change in the radial inertia forces of the vanes and the radial vane movement, which is not implemented in the model. Regarding the overall agreement of measurement and simulation confirms that the rotor torque and the wall shear stress are not able to close the gap between the simulation results and the experiments.

Figure 21 shows only the simulated and measured sound pressure levels of the pump at the blade passing frequency and the harmonics at k times 400 Hz. To visualize the trends, the sound pressure is normalized with the average value of the blade passing frequency and its harmonics. It can be seen that the trend of the sound pressure level at the blade passing frequency and its harmonics is captured correctly at most frequencies. However, a further enhancement of the simulation model and the test bench setup are necessary to achieve a better agreement between the measurements and the numerical results. Possible approaches to achieve this goal are to acoustically enclose the connected tubes at the test bench to reduce their contribution to the sound pressure level at the microphone. Another approach is to model the hydraulic circuit and the test device for the pump in the simulation. Nevertheless, this will lead to increased simulation times. For sure a combination of these approaches is possible, too.

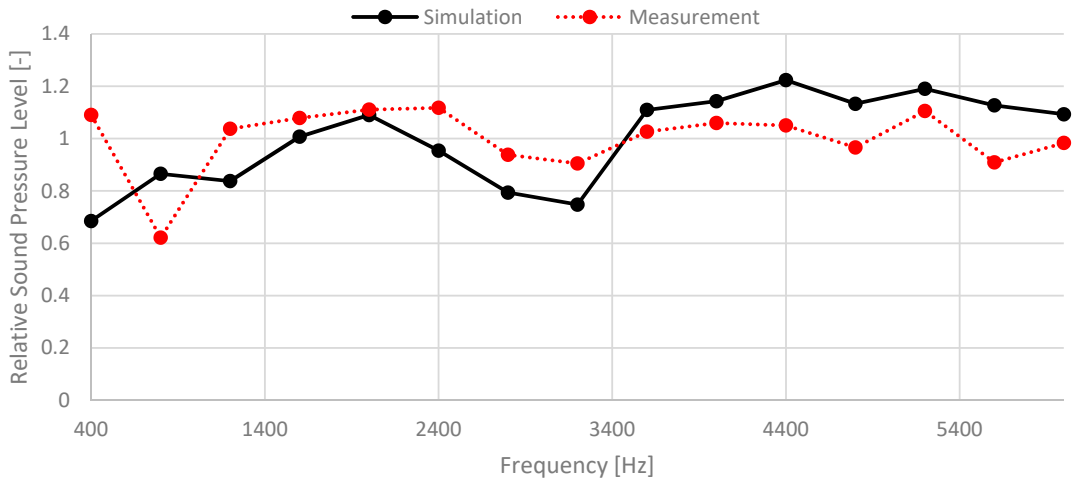

Figure 21. Normalized sound pressure level at blade passing frequencies of simulation and measurement for 2000 rpm and 15 bar.

4. Conclusions

A combined CFD-FEM approach to predict the noise radiation of a double stroke rotary vane pump for transmission applications was presented in this work. The CFD simulation model for the vane pump uses a morphing approach to model the moving parts. The developing pressure field in the pump as well as the wall shear stress were considered as noise sources of the fluid and used as load for the FEM model. In the FEM model the solution is obtained in the frequency domain in form of a frequency response analysis. To transfer the data from the CFD to the FEM grid a mapping approach is mandatory.

To ensure the correctness of the mapping approach the impact of mapping parameters and the impact of the mesh size on the mapping results have been investigated. To validate the mapping process the surface integral of the pressure field in the CFD simulations is evaluated and compared to the force sum in the FEM simulations. The results show that the mapping parameter *Maximum Distance* has the highest impact on the mapping results and has to be chosen according to the mesh size of the FEM and the CFD grid. Additionally, the impact of different angular positions of the pump rotor mesh have been investigated, since a morphing approach is used in the CFD simulation, which leads to a change in the element shape of the rotor mesh. This procedure also allows to draw conclusions for the mapping error depending on the transient pressure signal. If the mapping parameters are adapted correctly for the specific mesh size, a total error of less than 0.5% can be achieved. To avoid a loss of information, the mapping parameters were set to values, which led to slightly higher forces in the FEM model.

Within the scope of a study about the required length of the underlying time signal to obtain the correct excitation forces it was derived that one revolution of the pump is already sufficient to provide a reasonable resolution in the frequency domain. The reoccurring characteristic fluctuations of the excitation force could be captured within one revolution. This is due to the periodicity of the pump signal. Nevertheless, to get a better frequency resolution of the mapped forces and to enhance the resolution of the intermediate frequencies longer time signals can be taken into account, if the computational power and time is available. As a tradeoff between accuracy and computational time, it was decided to use the transient data of one full revolution of the pump with an angular resolution of 0.5° for the following investigations.

Different effects in the pump contribute to the noise radiation. Therefore, an investigation on the noise sources in the flow with the highest impact on the noise radiation of the pump was conducted. For this purpose, the static pressure field acting on the FEPS, the wall shear stress acting on the FEPS and the FRF have been taken into account. A force analysis derived that the pressure acting on the FEPS leads to the highest forces in the model. Here, the blade passing frequency and its harmonics show the highest force amplitudes. The locations where high forces are observed are located in the transition area of a displacement chamber from the suction to the delivery port or vice versa. The spatial extend of these locations matches with the angular extend of a displacement chamber. This is due to the pressure rise or drop within the displacement chamber during the transition. The forces resulting from the wall shear stress acting on the FEPS are small compared to the ones caused by the pressure field acting on the FEPS and lay within the magnitude of the mapping error of 0.5%. Consequently, the wall shear stress influence is neglected in this model.

Since the CFD model uses moving parts to model the pump function, one approach to take the FRF into account in the FEM simulation is to calculate a rotor torque from the pressure and wall shear stress acting on the moving surfaces. This torque was implemented as load in the FEM simulation at the mid position of the rotor in the rotor shaft. Additionally, the shaft was glued at the bearing positions to the housing to exaggerate the influence of the rotor torque. It was found that the impact of the FRF on the surface velocity of the pump housing is low for low rotation rates up to 2000 rpm. The magnitude of the surface velocity of the pump caused by the FRF is only 0.5% of the magnitude of the surface velocity caused by the pressure acting on the FEPS. Hence, the FRF is neglected for the

vibroacoustic simulation of this pump. This conclusion is depending on the pump type. For the investigated pump, the transversal location of delivery and suction ports reduces the forces which lead to a deflection of the rotor and hence, strongly reduces the bearing forces.

Finally, the acceleration and noise radiation of the pump were predicted by the vibroacoustic simulation at an operation condition of 2000 rpm and 15 bar. To validate the CFD simulation the pressure signal in a rotating displacement chamber was compared to measurements and showed a reasonable agreement. Subsequently, acceleration and sound pressure level measurements, which have been performed in a hemi-anechoic room, were compared to the predicted acceleration and sound pressure level at a microphone point in 96 mm distance to the pump. On the one hand, the results show a strong deviation for lower frequencies which can be traced back to the higher stiffness and less vibration-proneness of the model, due to the missing test device and the missing connecting tubes. On the other hand, it was shown that the trend of the sound pressure level at the blade passing frequency and its harmonics is in a reasonable agreement with the measurements.

Author Contributions: Concept T.H.; methodology T.H.; formal analysis/investigation T.H.; writing T.H.; review, editing and discussion G.B., T.L. and T.H.; supervision G.B. All authors have read and agreed to the published version of the manuscript.

Funding: This research received no external funding.

Acknowledgments: The authors would like to thank Jochen Abele for performing the measurements.

Conflicts of Interest: The authors declare no conflict of interest.

Nomenclature

Latin Symbols

A	surface [m]
c	speed of sound [m/s]
d	differential operatior [-]
$f_{bp,k}$	k-th blade passing frequency [1/s]
f_{max}	maximum resolvable frequency [1/s]
f_s	sampling frequency of a signal [1/s]
F	force [N]
k	positive integer [-]
n	rotational speed [1/s]
N_b	number of FFT bins [-]
N_e	number of elements per wave length [-]
N_{rev}	number of pump revolutions [-]
N_s	number of samples [-]
N_v	number of vanes [-]
p	static pressure [Pa]
R_{FRF}	ratio of surface velocity caused by FRF [%]
v_{FEPS}	surface velocity caused by pressure acting on FEPS [mm/s]
v_{FRF}	surface velocity caused by FRF [mm/s]

Greek Symbols

Δf	frequency resolution [1/s]
Δt	time step size [s]
$\Delta\alpha$	extend of acoustic fluid mesh [m]
$\Delta\beta$	acoustic element size [m]
$\Delta\gamma$	angular resolution [°]

Abbrevations

BEM	Boundary Element Method
CFD	Computational Fluid Dynamics
CMD	Conservative Maximum Distance
FEM	Finite Element Method
FEPS	flow enclosing pump surfaces
FRF	fluid rotor forces
MD	Maximum Distance
rpm	rounds per minute
URANS	unsteady Reynolds-Averaged-Navier-Stokes

References

1. Inaguma, Y.; Yoshida, N. Variation in Driving Torque and Vane Friction Torque in a Balanced Vane Pump. *SAE Tech. Pap. Ser.* **2014**, *1*, 1764.
2. Yoshida, N.; Inaguma, Y. Mathematical Analysis of Efficiencies in Hydraulic Pumps for Automatic Transmissions. *JTEKT Eng. J. Engl. Ed.* **2014**, *1011E*, 64–73.
3. Zouani, A.; Dziubinschi, G.; Marri, V.; Antonov, S. Optimal Vanes Spacing for Improved NVH Performance of Variable Displacement Oil Pumps; No. 2017-01-1062. In Proceedings of the SAE World Congress Experience (WCX), Detroit, MI, USA, 4–6 April 2017.
4. Ericson, L. On Fluid Power Pump and Motor Design, Tools for Noise Reduction. Ph.D. Thesis, Linköping University, Linköping, Sweden, 2011.
5. Carletti, E.; Miccoli, G.; Pedrielli, F.; Parise, G. Vibroacoustic Measurements and Simulations Applied to External Gear Pumps. An Integrated Simplified Approach. *Arch. Acoust.* **2016**, *41*, 285–296. [CrossRef]
6. Tang, C.; Wang, Y.S.; Gao, J.H.; Guo, H. Fluid-sound coupling simulation and experimental validation for noise characteristics of a variable displacement external gear pump. *Noise Control Engr. J.* **2014**, *62*, 123–131. [CrossRef]
7. Bonanno, A.; Pedrielli, F. A Study on the Structureborne Noise of hydraulic Gear Pumps. In Proceedings of the 7th JFPS International Symposium on Fluid Power, Toyama, Japan, 15–18 September 2008.
8. Woo, S.; Opperwall, T.; Vacca, A.; Rigosi, M. Modeling Noise Sources and Propagation in External Gear Pumps. *Energies* **2017**, *10*, 1068. [CrossRef]
9. Hoffmann de Mendonca, F. Structural Optimization in Acoustic Radiation. Master's Thesis, UTL, Instituto Superior Técnico, Lisboa, Portugal, 2007.
10. Miccoli, G.; Carletti, E.; Pedrielli, F.; Parise, G. Simplified methodology for pump acoustic field analysis: The effect of different excitation boundary conditions. In Proceedings of the INTER-NOISE 2016—45th International Congress and Exposition on Noise Control Engineering, Hamburg, Germany, 21–24 August 2016.
11. Mucchi, G.; Dalpiaz, G. Numerical vibro-acoustic analysis of gear pumps for automotive applications. In Proceedings of the 25th International Conference on Noise and Vibration engineering, Leuven, Belgium, 17–19 September 2012.
12. Opperwall, T.; Vacca, A. Modeling Noise Sources and Propagation in Displacement Machines and hydraulic Lines. In Proceedings of the 9th JFPS International Symposium on Fluid Power, Shimane, Matsue, Japan, 28–31 October 2014.
13. Schwarzer, S. Optimierung der Auslegung und des Betriebsverhaltens von hohlradgetriebenen Innenzahnradpumpen. Ph.D. Thesis, Technische Universität Ilmenau, Ilmenau, Germany, 2013.
14. Opperwall, T.; Vacca, A. *A Transfer Path Approach for Experimentally Determining the Noise Impact of Hydraulic Components*; SAE Commercial Vehicle Engineering Congress: Chicago, IL, USA, 2015.
15. Opperwall, T.; Vacca, A. A combined FEM/BEM model and experimental investigation into the effects of fluid-borne noise sources on the air-borne noise generated by hydraulic pumps and motors. *J. Mech. Eng. Sci.* **2013**, *228*, 457–471. [CrossRef]
16. Pan, Y.; Li, Y.; Huang, M.; Liao, Y.; Liang, D. Noise source identification and transmission path optimization for noise reduction of an axial piston pump. *Appl. Acoust.* **2018**, *130*, 283–292. [CrossRef]
17. Liu, H.; Ding, J.; Huang, M.; Dai, H.; Tan, M.; Tang, X. Numerical Research on Hydraulically Generated Vibration and Noise of a Centrifugal Pump Volute with Impeller Outlet Width Variation. *Math. Probl. Eng.* **2014**, *2014*, 620389. [CrossRef]
18. Si, Q.; Wang, B.; Yuan, J.; Huang, K.; Lin, G.; Wang, C. Numerical and Experimental Investigation on Radiated Noise Characteristics of the Multistage Centrifugal Pump. *Processes* **2019**, *7*, 793. [CrossRef]
19. Hwang, J.; Kim, J.; Yoon, T.; Kim, H. Comparison of the FSI Analysis Results of the Vane Pump According to the software. *ICIC Int.* **2018**, *9*, 789–795.
20. Hieronymus, T.; Lobsinger, T.; Brenner, G. Investigation of the Internal Displacement Chamber Pressure of a Rotary Vane Pump. *Energies* **2020**, *13*, 3341. [CrossRef]
21. Simcenter Nastran 2019.2 User Documentation. Available online: https://docs.plm.automation.siemens.com/tdoc/scnastran/2019_2/help/#uid:index (accessed on 2 October 2020).

22. Willie, J. Use of CFD to predict trapped gas excitation as source of vibration and noise in screw compressors. In Proceedings of the 10th International Conference on Compressors and Their Systems, London, UK, 11–13 September 2017.
23. Lobsinger, T.; Hieronymus, T.; Brenner, G. A CFD Investigation of a 2D Balanced Vane Pump Focusing on Leakage Flows and Multiphase Flow Characteristics. *Energies* **2020**, *13*, 3314. [CrossRef]